Sensitivity of MCS Low-Frequency Gravity Waves to Microphysical Variations

Rebecca D. Adams-Selin*

Atmospheric and Environmental Research, Inc.

**Corresponding author address:* Atmospheric and Environmental Research, 11515 South 39th St, Suite 102, Bellevue, NE 68123

E-mail: rselin@aer.com

Early Online Release: This preliminary version has been accepted for publication in *Journal of the Atmospheric Sciences*, may be fully cited, and has been assigned DOI 10.1175/JAS-D-19-0347.1. The final typeset copyedited article will replace the EOR at the above DOI when it is published.

ABSTRACT

The sensitivity of low-frequency gravity waves generated during the development and mature stages of an MCS to variations in the characteristics of the rimed ice parameterization were tested through idealized numerical simulations over a range of environment shears and instabilities. Latent cooling in the simulations with less dense, graupel-like rimed ice was more concentrated aloft near the melting level, while cooling in simulations with denser, hail-like rimed ice extended from the melting level to the surface. However, the cooling profiles still had significant internal variability across different environments and over each simulation's duration. Initial wave production during the MCS developing stage was fairly similar in the hail and graupel simulations. During the mature stages, graupel simulations showed stronger perturbations in CAPE, due to the cooling and associated wave vertical motion being farther aloft; hail simulations showed stronger perturbations in LFC due to cooling and wave vertical motion being concentrated at lower levels. The differences in the cooling profiles were not uniform enough to produce consistently different higher order wave modes. However, the initiation of discrete cells ahead of the convective line was found to be highly sensitive to the nature of the prior destabilizing wave. Individual events of discrete propagation were suppressed in some of the graupel simulations due to the higher location of both peak cooling and vertical wave motion. Such results underscore the need to fully characterize MCS microphysical heating profiles and their low-frequency gravity waves to understand their structure and development.

Accepted for publication in *Journal of the Atmospheric Sciences*. DOI10.1175/JAS-D-19-0347.1.

1. Introduction

Low-frequency gravity waves generated by variations in the diabatic heating profile produced by ongoing convection impact both the surrounding environment and the convection acting to generate them (e.g., Bretherton and Smolarkiewicz 1989; Nicholls et al. 1991; Pandya et al. 1993; Mapes 1993; Shige and Satomura 2001; Lane and Reeder 2001). Because of their low frequency, these waves can propagate horizontally for some distance without their energy escaping vertically (Pandya et al. 2000), thereby affecting the stability and shear of the surrounding environment. Recent work by the author found low-frequency waves generated by idealized Mesoscale Convective Systems (MCSs) produced perturbations in Convective Available Potential Energy (CAPE) of as much as 60%, and of 0-5 km shear of 50% or greater of the original value (Adams-Selin 2020, AS20 hereafter). That work also found extended periods of intensification of the convective updraft during the mature stage of the MCS to be directly connected to episodes of discrete propagation (Fovell 2002; Fovell et al. 2006) where the low-frequency waves "prepared" the area in advance of the system with gradual ascent over a large area, and subsequent high-frequency waves directly initiated new convective cells in advance of the already existing convective line. Work by Pandya and Durran (1996) and Pandya et al. (2000) has also found these low-frequency waves can generate the in- and extra-storm circulation found within mature MCSs including front-to-rear flow overlying rear-to-front inflow. However, those studies chose to use a steady-state thermal forcing profile from a mature MCS as a way to underscore the importance of low-frequency waves. To this date, no studies have examined how low-frequency waves generated from latent heating profiles evolving during a developing MCS impact its extra- and in-storm circulation.

Low frequency waves are typically identified by the vertical mode of the diabatic heating generating them. For example, an $n = 1$ wave is generated by an increase in heating over the depth of the

Accepted for publication in *Journal of the Atmospheric Sciences*. DOI10.1175/JAS-D-19-0347.1.

troposphere with a peak in the mid-levels, similar to diabatic heating within a convective line as condensation and updraft speed peaks in the mid-levels (Nicholls et al. 1991; Gallus and Johnson 1991). An $n = 2$ profile associated with convection consists of heating aloft with cooling in the lower half of the troposphere, similar to the heating profile of a stratiform region (Gallus and Johnson 1991). As the MCS diabatic heating profile is the generating source of these waves, it would follow that uncertainties in the diabatic heating profile could modify the structure and timing of the gravity waves and thereby impact the surrounding environment. Yet MCS diabatic heating profiles are difficult to model successfully, particularly given the notorious sensitivity of MCS structure to microphysical parameterization choices (e.g., Nicholls 1987; Fovell and Ogura 1988; Szeto and Cho 1994; Yang and Jr. 1995; Bryan and Morrison 2012; Van Weverberg et al. 2012; Adams-Selin et al. 2013b; Morrison et al. 2015b; Jensen et al. 2018; Pu et al. 2018). The high sensitivity of convective development to the parameterization of rimed ice is a specific concern, including choices made about the density, mean size, and fall speed of the rimed ice. Frequently in the literature this sensitivity is studied through modifying the rimed ice category in the microphysical parameterization to be more similar to graupel, with a smaller density and mean size and slower fall speed, or more like hail, with a larger density, larger mean size, and faster fall speed. Previous studies examining this effect initially appear conflicted. For example, van den Heever and Cotton (2004), Cohen and McCaul (2006), Adams-Selin et al. (2013b), and Adams-Selin et al. (2013a) all found convective simulations with graupel-like rimed ice to have stronger cold pools due to larger surface area to volume ratio and slower fall speed resulting in more of the graupel melting before reaching the surface. Conversely, Van Weverberg et al. (2011), Van Weverberg et al. (2012), Morrison and Milbrandt (2011), and Morrison et al. (2015a,b) found convective simulations with graupel-like rimed ice to have weaker cold pools, as the slower particle fall speed ensured a higher concentration of rimed ice particles remained aloft above the melting layer. However, further

Accepted for publication in *Journal of the Atmospheric Sciences*. DOI10.1175/JAS-D-19-0347.1.

work has reconciled these differences by determining the relative impacts of rimed ice sensitivity differ - and can even change sign - across environments with varying stabilities and depending on the length of the simulation. Van Weverberg (2013) noted that as simulations progressed in time the differences between squall line simulations with hail or graupel lessened as the slower-falling graupel eventually fell below the melting level. Van Weverberg (2013) and (Morrison et al. 2015b) both found hail-graupel sensitivities were much smaller in low-CAPE simulations than high-CAPE simulations. The relative humidity of the environmental profile also played a role, determining if the graupel hydrometeors aloft were able to sublimate and evaporate, leading to further cooling (Van Weverberg 2013).

The parameterization of rimed ice naturally is a key factor in the MCS hydrometeor distribution and latent heating and cooling profiles. The horizontal width of the convective and stratiform regions, both in sum and in relation to the other, are directly impacted. Given the variations in fall speeds, the parameterization controls how quickly rimed ice descends to the surface as well as the vertical distribution of melting and the speed at which it develops. With graupel-like rimed ice, its slower fall speed ensured it was advected rearward before reaching the melting level, spreading the cooling by melting over a larger horizontal area (Jensen et al. 2018) but more vertically concentrated near the melting level (Adams-Selin et al. 2013b; Morrison et al. 2015a).

Thus, variations in how rimed ice is parameterized highly impact the hydrometeor structure and diabatic heating profiles of MCSs, and the diabatic heating profile acts to generate low-frequency gravity waves that modify the environment - including the rear-to-front flow - around the MCS and feed back to the intensity and structure of the MCS itself. Previous studies on MCS microphysical sensitivities have been focused on in-storm impacts alone; this study will expand analysis to the low-frequency gravity waves generated by the diabatic heating profile and their surrounding environmental impacts. Previous low-frequency waves studies (e.g., Pandya and Durran 1996; Pandya

Accepted for publication in *Journal of the Atmospheric Sciences*. DOI10.1175/JAS-D-19-0347.1.

et al. 2000) have focused on the waves generated from steady-state, mature storm latent heating profiles and how tilts in the profiles impact the generated waves and subsequent intra- and extra-storm circulation. This work broadens that research by examining gravity wave generation from time-varying latent heating profiles of a developing MCS, as well as how differing diabatic heating profiles affect the environmental fields surrounding the storm. It also furthers the results of AS20 by examining the sensitivity of low-frequency gravity wave impacts on surrounding environmental shear and stability to rimed ice characteristics, and how those sensitivies feed back to MCS intensity and structure. As previous studies have observed rimed ice parameterization sensitivities are highly dependent upon the initial environment, this study will also examine simulations with different initial stabilities and shears.

Section 2 presents the experiment and model design for this study. The sensitivities of the MCSs to rimed ice modifications are detailed in Section 3, and the differences in generated low-frequency waves and their subsequent impacts on MCS maintenance and intensity are shown in Section 4. Discussion and conclusions follow in Section 5.

2. Methodology

Idealized Cloud Model 1 version 18 (CM1; Bryan and Fritsch (2002)) simulations were used in this study to complement those conducted as part of AS20. Similar to that study, a modified version of the Weisman and Klemp (1982) sounding was used with the Brunt-Väisälä frequency profile smoothed to eliminate trapping levels. A 350 km (x direction) by 300 km (y direction) by 18 km (z direction) domain was used with horizontal grid-spacing of 250 m and vertical grid-spacing of 100 m. Convection was initialized via the "cold pool-dam break" method (Weisman et al. 1997), consisting of a rectangular box of negative 6K potential temperature perturbation established during initiation. The Morrison microphysical parameterization (Morrison et al. 2009)

Accepted for publication in *Journal of the Atmospheric Sciences*. DOI10.1175/JAS-D-19-0347.1.

was used with the reflectivity calculation specific to that scheme. The rimed ice category was varied by running simulations with either hail or graupel. This method was chosen to align with many previous studies (e.g., Morrison et al. 2015b,a; Van Weverberg 2013; Pu et al. 2018). All vertical cross-section results presented will be from the Y=125 km cross-section, with a 10-km average of values about that line.

In order to examine impacts of CAPE and shear perturbations, the initial sounding was modified. Initially, three different mixing ratios (12.2, 14.3, and 16.2 g kg^{-1}) over the surface to the LCL were used to produce initial Maximum Unstable Convective Available Potential Energy (MUCAPE) values of approximately 1500, 2500, and 3500 J kg^{-1}. The hail and graupel simulations in the environment of 1500 J kg^{-1} CAPE showed very few, if any, differences in the resulting hydrometeor distribution and the waves produced. This result agrees with previous studies that found MCS sensitivity to hail-graupel modifications was small in environments with low instability (Morrison et al. 2015b; Van Weverberg 2013). However, while the simulations with initial surface mixing ratios of 14.3 and 16.2 g kg^{-1} (2500 and 3500 J kg^{-1} MUCAPE) did show differences, the general trends of MCS structure, latent cooling profile, and wave generation were not significantly different particularly compared to the differences caused by the shear or hail/graupel modifications. In the interest of space, only simulations with one initial instability (16.2 g kg^{-1} surface mixing ratio or 3500 J kg^{-1} MUCAPE) will be presented here, although comments about where the results of the instability tests differed from those shown will be provided in the text. The environmental shear over the 0-5 km layer consisted of 5, 15, or 25 m s^{-1} “westerly” surface winds relaxing to 0 m s^{-1} at 5 km. A list of all the simulations is provided in Table 1.

Accepted for publication in *Journal of the Atmospheric Sciences*. DOI10.1175/JAS-D-19-0347.1.

3. Gross MCS sensitivity to hail-graupel modifications

The general structure of the MCSs in each of the initial environments is detailed in AS20. Generally, systems in environments with weak shear - with the rimed ice category hail or graupel - had weaker updrafts, a trailing stratiform region, and propagated slowly forward at speeds of 5-10 m s^{-1}. The systems in middling shear exhibited stronger updrafts, produced a large trailing stratiform region, and remained largely stationary. The systems in strong shear produced large leading stratiform regions, and propagated rearward in the domain at a speed of approximately 11 m s^{-1}. Systems in environments with larger initial instability produced stronger updrafts, as expected.

a. Hydrometeor distribution

The most noticeable microphysical differences between the hail and graupel simulations are hydrometeor distribution between the convective and stratiform regions, and the resulting reflectivity profiles. The variations in the total reflectivity profiles over the length of all the 2.5-h simulations are highlighted in Figure 1. Immediately evident are the differences in peak reflectivities at and below the melting level (just below 4 km). Hail simulations have a wider distribution of reflectivities in the lower levels with peak frequencies occurring from reflectivities of 25 to 55 dBZ with a relative minimum around 45 dBZ (Figs. 1a,c,e). Such a pattern corresponds to a thin but intense (>50 dBZ) convective line, followed by a stratiform region with low reflectivities. Conversely, the graupel simulations have a narrower frequency distribution with most of the low-level reflectivities around 45 dBZ, corresponding to a broad convective line of lesser intensity (Figs.1b,d). In the high-shear simulations (Figs. 1e,f), the low-level hail and graupel differences are still evident, but both simulations have a larger fraction of the low-level reflectivities occurring around 35 dBZ (i.e., the stratiform region). The frequencies shown in Fig. 1 are normalized by total reflectivity occur-

Accepted for publication in *Journal of the Atmospheric Sciences*. DOI10.1175/JAS-D-19-0347.1.

rence at each height, so the large leading stratiform region produced in the high-shear simulations reduced the normalized frequency of reflectivities in either convective line.

The mean vertical profiles of the different hydrometeor mixing ratios over the horizontal domain and time duration of each simulation, shown in Fig. 2, further corroborate this assessment. Below the melting level the hail simulations show higher mean rain water mixing ratios over the 0-1 km layer, as well as larger mean hail/graupel mixing ratios over the 1-3 km layer, corresponding to the more intense reflectivities seen in the hail simulations in those layers. The smaller graupel hydrometeors melt more quickly as they descend below the melting level, transitioning more quickly to smaller rain drops. The smaller rain drops also evaporate more quickly, contributing to the lower 0-1 km rain mixing ratios in the graupel simulations.

Above the melting level, the hail-graupel differences can again be largely explained by the graupel simulations having a very broad convective line of relatively lower reflectivities, with minimal distinction between the convective line and the stratiform region. The hail simulations, particularly in the environments with middling or high shear, have wide regions of snowflakes advected away from the convective line in upper levels, corresponding to the lower reflectivities aloft seen in Figs. 1a,c,e. The mixing ratio profiles similarly show larger mean mixing ratios of snowflakes aloft in the hail than in the graupel simulations (c.f., Figs. 2a,b). The larger hailstones remain near the convective line, resulting in smaller overall mean hail mixing ratios. Conversely, the smaller graupel and snow hydrometeors are advected over a larger area, resulting in larger overall mean mixing ratios. The high shear simulations show the largest differences in reflectivity (Figs. 1e,f) and mean graupel/hail mixing ratio (Figs. 2e,f) above the melting level. The amount of snow aloft shown in the vertical profiles in the high shear hail and graupel simulations is about equivalent; almost the entire contrast lies in the distribution of the graupel (Figs. 2e,f). The simulations with weaker shear (Figs. 1a-d) show less of a contrast. These results are robust across multiple insta-

Accepted for publication in *Journal of the Atmospheric Sciences*. DOI10.1175/JAS-D-19-0347.1.

bilities with simulations in larger instability producing more condensate include rimed ice aloft, similar to the studies of Van Weverberg (2013) and Morrison et al. (2015b).

In addition to the mean vertical profiles in Fig. 2, it is also instructive to examine the evolution over time of the 90th percentile of the graupel/hail mixing ratio (Fig. 3). These figures show that graupel simulations not only produce more rimed ice aloft than the hail simulations, the 90th percentile mixing ratio magnitudes are also larger. Again, this result is due to the smaller graupel particles being lofted higher and falling more slowly, despite potentially being advected farther from the convective updraft. However, the hail simulations do produce hail amounts that occasionally are of the same magnitude as those of the graupel simulations, particularly during the first 30 min of the simulation during the initial development of the convective core. The initial availability of roughly equivalent amounts of rimed ice in both the hail and graupel simulations becomes an important fact in the evolution of the simulations' latent cooling profiles, discussed in the next section. Simulations in environments with more shear loft more rimed ice during initial development of the convective updraft, be the ice hail or graupel, likely due to the stronger updraft that is initially produced (see Fig. 9 of AS20). After the initial updraft development, however, the high shear systems show smaller 90th percentile magnitudes of rimed ice aloft compared to the middling shear simulations. From Fig. 2 it can be seen that the total amount of rimed ice above the melting level is about equivalent between middling and high shear simulations, but the values in Fig. 3 for high shear are smaller because the rimed ice is distributed over a larger region due to the stronger environmental flow.

b. Latent heat distribution

Given the different hydrometeor distributions, variations in the simulations' latent cooling profiles (Fig. 4) naturally follow. Figure 4 displays latent cooling by process (left two columns) and

Accepted for publication in *Journal of the Atmospheric Sciences*. DOI10.1175/JAS-D-19-0347.1.

in sum (right two columns). Many of the differences agree nicely with previous research (e.g., Adams-Selin et al. 2013b; Morrison et al. 2015b). Onset of cooling, both by evaporation as rain falls below cloud base, and by sublimation and melting as rimed ice falls through and below the melting level, occurs slightly more quickly in the hail simulations due to the faster fall speed of its rimed ice. After the graupel begins falling below the melting level, cooling rate variations among hail and graupel simulations become dependent on the environment. At that point (40-60 min into the simulations, depending on environment and rimed ice species) in the middling shear simulations the total microphysical cooling in the hail simulation (16.2H15) is larger than the graupel simulation (16.2G15). However, in the weak and strong shear, the total microphysical cooling in the graupel simulations (16.2G5, 16.2G25) is larger than in the hail (16.2H5, 16.2H25). The differences are almost entirely due to sub-melting layer rainfall evaporation. In the high and low shear simulations, evaporation rates are larger in the graupel than in the hail simulations; in the middling shear evaporation rates are larger in the hail simulation. This result can also be seen when comparing the mean rain mixing ratio profiles in Figs. 3c and d. These results are robust across both tested instabilities, although all simulations in larger instability have stronger cooling rates due to more condensate being lofted, similar to AS20.

The latent cooling profiles also follow similar patterns if analyzed by process. In all shears, the graupel in the graupel simulations melts more quickly once falling below the melting level, concentrating cooling from melting vertically near the melting level. Mean melting rates in the graupel simulations, due to their vertical concentration, are larger than the rates seen in the corresponding hail simulations despite the hail and melting in the hail simulations being more concentrated horizontally. Cooling rates due to sublimation are also larger in magnitude in the graupel than hail simulations across all environments, extend approximately 2 km farther into the upper levels, and do not extend below the melting level. Cooling by sublimation in the hail simulations extends up

Accepted for publication in *Journal of the Atmospheric Sciences*. DOI10.1175/JAS-D-19-0347.1.

to 2 km below the melting level, with simulations in larger instability or stronger shear extending farther.

In sum, cooling in the hail simulations starts anywhere from 10-30 min before cooling in the graupel simulations, allowing for faster cold pool and subsequent updraft development. However, once rimed ice begins falling below the melting level in both simulations, cooling rates for all processes are larger in the graupel simulation than in the hail simulations, with the exception of evaporative and total cooling in simulations with 15 m s^{-1} shear (c.f. Figs. 4c,d). The vertical location of the total cooling maxima is also farther aloft in the graupel simulations than hail simulations, between approximately 3-6 km as opposed to 2-4 km, regardless of environment.

The vertical distribution of the contributions by process generally agree with the mean latent cooling rate behavior of MCSs analyzed by Marinescu et al. (2016). That study used a complex bin-emulating microphysical parameterization allowing both graupel and hail to co-exist along with three other ice and three liquid hydrometeor classes. Their simulations compared favorably to radar-gauge precipitation estimates, radar-based analysis of updraft speed, and subjective evaluation of storm evolution; that simulations of this study show similar microphysical trends is reassuring. Both the simulations of this study and those of Marinescu et al. (2016) found the contributions to cooling from melting increasing with time in both the convective and stratiform regions. Marinescu et al. (2016) did find that the convective line cooling rate contributions from evaporation and sublimation slowly decreased with time starting about 2 hours after maturity, and stratiform region contributions lessened about 3 hours after maturity (e.g., see their Fig. 10). In this study the evaporation and sublimation rates continue to increase throughout the simulations, but their duration only continues to about 1.5 hours after maturity.

Accepted for publication in *Journal of the Atmospheric Sciences*. DOI10.1175/JAS-D-19-0347.1.

4. Gravity wave generation and impacts

Given the highly variable nature of the latent heating profiles within these simulations, wave activity covering a range of different frequencies and wave modes was produced. Furthermore, given the long-lasting nature of low frequency waves, as multiple waves are generated their signatures when propagating in advance of the convective system would overlap and interact. In order to identify low frequency waves and their mode objectively, the following criteria were required as in AS20. The wave mode, n, was determined by the wave speed and a subsequently described Fourier decomposition method of the generating latent heating profile. Wave speed and n are related through the relationship $c = NH/n\pi$, where c is the wave speed and H the vertical depth of the troposphere (Nicholls et al. 1991). The wave signature in the vertical motion field must also agree with the determined wave mode and be long-lasting, although it is possible the signature might disappear temporarily while interacting with another wave.

a. Waves and generating processes

Waves associated with an $n = 1$ heating profile extending the depth of the atmosphere as convection initially develops appear first in all simulations. Vertical motion at 6 km, where wave theory predicts vertical motion associated with these waves should be largest, is displayed in a Hovmöller diagram in Figs. 5a-f. Also identified in Fig. 5 are paths of the waves as the propagate through the environment. The identified paths were determined using cross-sections of vertical motion over time along with Fig. 5. In AS20, an $n = 1$ wave was generated by each development of a new convective updraft and surge in latent heating in the mid-levels (e.g., their Fig. 5). To confirm the $n = 1$ wave generation seen here correspond with similar latent heating surges, the mean vertical heating profile was smoothed with a 1-2-1 filter and then decomposed into 10 Fourier components similar to Stephan et al. (2016) and as in AS20. The A_1 Fourier coefficient is associated with an

Accepted for publication in *Journal of the Atmospheric Sciences*. DOI10.1175/JAS-D-19-0347.1.

$n = 1$ mode. The values of the coefficient are plotted in Fig. 6 if both the coefficient is determined to be 99% significant per a two-tailed t-test, and the entire decomposition is determined to be 99% significant per the F-statistic. The early peaks in the A_1 coefficient clearly correspond to generation times of the early $n = 1$ waves. While it is likely more $n = 1$ waves are generated later in each simulation, any potential signals in the vertical motion field (Fig. 5) are obscured by higher wave modes. Few differences appear among number, strength, or timing of $n = 1$ waves generated in the hail and graupel simulations. This early in each simulation, the differences engendered by the different rimed ice classes do not yet make themselves apparent. As noted in AS20, the $n = 1$ waves are generated more quickly in the simulations with higher instability and/or shear.

Hovmöller diagrams of vertical motion at 2.5 km are useful for identifying higher order waves modes such as $n = 2$ and $n = 3$ (Figs. 5g-l). The A_2 and A_3 Fourier coefficients are also plotted in Fig. 4g-l. The first $n = 2$ waves appear only a few minutes earlier in the hail than the graupel simulations. From Fig. 4, it can be seen that the first $n = 2$ waves appear shortly after evaporative cooling rates first start to increase as rain water first descends below the cloud base. At this point the differences in the hail and graupel simulations are still minimal.

The second $n = 2$ wave appears in these simulations as the stratiform region begins to expand, as in AS20. Fig. 7 displays vertical cross-sections of latent heating and cooling along with total condensate from before (a,d,g,j,m,p) and after (b,e,h,k,n,q) initial development and expansion of the stratiform precipitation region in each simulation. In light shear, melting and sublimation in the graupel simulations are more concentrated vertically near the melting level, while in the hail simulation these processes extend over a deeper layer to lower vertical levels (Fig. 4; c.f., Figs. 7b,e). Hence, the 2nd $n = 2$ wave generated in 16.2H5 similarly extended over deeper layers than the same wave in the graupel simulations. For example, note the $n = 2$ wave vertical motions

Accepted for publication in *Journal of the Atmospheric Sciences*. DOI10.1175/JAS-D-19-0347.1.

in 16.2H5 (see the arrow in Fig. 7c) extended from 6 km to the surface. Conversely, in 16.2G5 vertical motions only extended to 4 km.

In the middling and strong shear simulations, latent cooling during the 2nd $n = 2$ wave generation time in the graupel simulations does not even have a significant $n = 2$ signal per the A_2 coefficient (Fig. 4j,l) with cooling mainly concentrated above 6 km due to sublimation (Fig. 4d,f). A weak $n = 2$ wave does appear in these graupel simulations (see arrows in Fig. 7l, r), but associated vertical motions are not as strong and do not extend over as deep a layer as those wave generated in the hail simulations (Fig. 7i, o). Review of the latent heating profile reveals the weak $n = 2$ waves in the graupel simulations were instead generated by a slight decrease in latent heating over the lower half of the troposphere (noted by blue arrows in Fig. 6d, f).

The third higher order wave appears in all simulations at the same time a rear inflow jet strengthens, as seen in Figs. 8 and 9 and in AS20. Sublimation and evaporation rates increase as the rear inflow increases, leading to a surge in cooling (Figs. 8b,e,h,k,n,q and 4). In the light shear cases, inflow and mid-level cooling are both slightly stronger in 16.2G5; the resulting $n = 2$ wave is associated with slightly stronger upward vertical motion as well (Figs. 8c, f). In middling shear the different vertical distributions of the cooling become more important. At 65 min, the time of the generation of the third higher order wave in 16.2H15, Fig. 4c shows sublimation descending to 3 km, melting to 2 km, and larger evaporation values almost to the surface. Meanwhile, at 70 min in 16.2G15 (Fig. 4d) sublimation values are concentrated around 6 km aloft (instead of 4 km in 16.2H15), melting is only evident to 3 km, and evaporation rates are about 0.5 K h^{-1} smaller in magnitude. As a result, the third wave generated in 16.2H15 is a $n = 2$ wave with peak vertical motions of 0.25 m s^{-1} extending below 2 km (Fig. 8i). The third wave in 16.2G15, conversely is an $n = 3$ wave with peak motions confined above 3 km. A similar result is evident in heavy shear. In 16.2H25 cooling associated with rear inflow from the "east" extends from 7 km to the surface

Accepted for publication in *Journal of the Atmospheric Sciences*. DOI10.1175/JAS-D-19-0347.1.

(Fig. 8n) and the resulting $n = 2$ wave similarly extends up to 7 km; in 16.2G25 cooling is instead concentrated from 2 km up to the anvil and peak $n = 2$ wave vertical motions do not extend below 2 km.

b. Rear-to-front flow

Dry simulations, conducted by PD96 and Pandya et al. (2000), driven by smoothed, steady-state, time-averaged latent heating fields from a mature MCS were able to recreate the traditional storm-scale flows within an MCS, including front-to-rear flow ascending from the surface to upper levels, and rear-to-front flow descending from mid-levels to the surface. These flows were generated by a combination of $n = 1$ and $n = 2$ gravity waves generated from the latent heating profiles. The mid-level rear-to-front flow in particular was induced by $n = 2$ waves, although PD96 noted that the shape and tilt of the latent heating profile impacted the strength and vertical placement of the rear-to-front flow field. Cooling located rearward of the convective heating appeared key to the rear-to-front flow descending to the surface behind the convective line (Figs. 20a,c of PD96); a tilted heating/cooling profile pair resulted in stronger rear-to-front flow than an upright profile (e.g., compare their Figs. 20a and c, or Figs. 20b and d). The simulations conducted here feature hydrometeors, meaning rear-to-front flow could additionally be enhanced by a low mid-level pressure gradient induced by the warm stratiform region overlying the microphysically cooled surface cold pool. However, coherent wave-like perturbations in the u wind field are evident propagating rearward past the stratiform region (not shown), strongly hinting that the flow fields in this "moist" simulation are similarly being driven by low-frequency gravity waves.

From Fig. 9 the generation times of the $n = 2$ waves are plotted in conjunction with maximum values of rear-to-front flow rearward of the convective line with respect to time (note in 16.2H25 and 16.2G25, "rearward" is to the right of the convective line, in the leading stratiform region, and

Accepted for publication in *Journal of the Atmospheric Sciences*. DOI 10.1175/JAS-D-19-0347.1.

"rear-to-front" flow travels from the east or from larger X values). At the time of the generation of the first $n = 2$ wave, when precipitation and associated cooling first descend below cloud level, there is no response in the rear-to-front flow field in the strong shear simulations (Figs. 9e,f). The rear-to-front flow in the weak and middling shear simulations (Figs. 9a-d) shows a slight response largely concentrated around 1-2 km. Figs. 10a, b show u wind and latent heating and cooling cross-sections at the generation time of the first $n = 2$ wave in 16.2H15 and 16.2G15. (Profiles from16.2H5 and 16.2G5 are similar.) The rear-to-front flow is largely concentrated below 2 km and within 20 km of the updraft. The heating profile at this time is similar to that shown in Fig. 20c of PD96: heating from the upright updraft extending the depth of the troposphere, and cooling located over the lower third of the troposphere slightly rearward of the updraft; this profile is similar to that produced by a cell when it first produces precipitation. The u wind response PD96 saw from this profile is also similar to the response seen here: the strongest rear-to-front flow concentrated close to the updraft and in the lowest 2 km. It should be noted that the PD96 u wind response shown in their Fig. 20 is from 6 h after simulation start and extends up to 200 km rearward of the source heating and cooling. Here the u wind response is largely confined within 25 km but is from only 24 min into the simulation, so any generated $n = 2$ wave has not been able to propagate over as large an area. The comparison of these simulations and PD96 results suggests that the first $n = 2$ wave did not act to generate mid-level rear-to-front flow in the simulations, as observed in Fig. 9, because of the shape of the associated latent heating profile.

The second $n = 2$ waves in this study's simulations were generated when the MCSs begin to develop stratiform precipitation, as shown in Fig. 7. The light shear simulations (16.2H5 and 16.2G5; Figs. 7b,e) show a tilted heating and cooling profile, similar to Fig. 20a of PD96, with the cooling rearward of the heating. Both here and in the similar profile in PD96 the rear-to-front flow descends to the surface and extends over 50 km behind the convective line. The cooling in

Accepted for publication in *Journal of the Atmospheric Sciences*. DOI10.1175/JAS-D-19-0347.1.

16.2H5 and rear-to-front flow are both maximized lower aloft, around 2-4 km, while the cooling and rear-to-front flow in 16.2G5 are both maximized farther aloft, near 5 km, due to the slower fallspeed of the graupel compared to hail. This distinction between the vertical location of the rear-to-front flow maxima is evident in Figs. 9a,b, which also shows that mid-level rear-to-front flow appears in both simulations after generation of the second $n = 2$ wave.

At the time of the second $n = 2$ wave in the middling shear simulations (16.2H15, Fig. 7h; and 16.2G15, Fig. 7k), the updraft heating profile is still upright with the latent cooling appearing rearward of the updraft at lower levels, similar to the PD96 profile shown in their Fig. 20c and even the latent heating/cooling profile at the generation time of the first $n = 2$ wave (Figs. 10a,b). The rear-to-front flow does extend farther rearward at the time of the second $n = 2$ wave than in Figs. 10a,b, but is still strongest below 2 km. The high shear simulations similarly have very upright heating and cooling profiles and weak, elevated rear-to-front flow (Figs. 7n, q).

The latent heating profiles at the generation time of the third $n = 2$ wave are associated with an increase in rear inflow (Fig. 8). The middling shear latent heating profiles have evolved. Simulation 16.2H15 shows a tilted heating/cooling profile with cooling extending from 8 km all the way to the surface (Figs. 8h). Much like the simulation with tilted heating/cooling profile with rearward-displaced cooling in Fig. 20a of PD96, the 16.2H15 u wind field descends to the surface, is maximized near the cooling around 2 km, and extends rearward behind the convection. From Fig. 9c we can see that this overall vertical structure of the rear-to-front flow is consistent for the rest of the simulation. Conversely, the cooling values in 16.2G15 (Fig. 8k) are split into two: one larger maxima located around 6.5 km, largely associated with sublimation, and another smaller maxima between 0-2 km due to evaporation (Fig. 4d). This latent profile partially mimics the upright heating/cooling profile of Fig. 20a of PD96, and the rear-to-front flow does show a maxima between 0-2 km largely remaining close to the cooling. With the addition of cooling around 6 km,

Accepted for publication in *Journal of the Atmospheric Sciences*. DOI10.1175/JAS-D-19-0347.1.

an additional peak in rear-to-front flow is evident aloft at that point, but the u wind response does not extend rearward. The vertical motions associated with the $n = 3$ wave generated by the 6-km cooling would actually weaken any rear-to-front flow at 4 km, instead intensifying flow around 8 km. Perhaps the combination of the $n = 3$ circulation induced by the 6 km cooling, and the more surface-based rear-to-front flow induced by the shape and tilt of the $n = 2$ latent heating/cooling profile, combined to produce the weak 4 km rear-to-front flow seen in 16.2G15. The 3-4 km rear-to-front flow displayed in Fig. 9d remains weak until almost 120 minutes into the simulation. Strongly increased rates of evaporation extending over 0-3 km depth also began to develop at that point (Figs. 4d).

Finally, from Fig. 9e,f it is evident that the rear inflow in the strong shear simulations never descends to the surface outside of the storm itself. This is somewhat contrary to previous analyses such as those conducted by Pettet and Johnson (2003). The latent cooling profile in 16.2H25 (Fig. 8n) has begun to tilt slightly, and the resulting waves appear to be strengthening the mid-level rear inflow aloft, albeit it is still quite weak outside of the storm (Fig. 8o). The heating and cooling profiles in 16.2G25 are unique with cooling almost entirely concentrated between 3 and 8 km; no simulations in PD96 addressed such a profile. Little response in the u wind field is seen outside of the storm in this simulation (Fig. 8r). It is likely that a cooling profile unfavorable for $n = 2$ waves aided this weaker response.

In sum, the development of the mid-level rear inflow in all simulations is tightly correlated with the placement and tilt of the latent heating and cooling profiles. The structure of the inflow, particularly the location of any maxima in the vertical and its extent rearward, appears to be largely determined by higher order wave modes generated by latent heating and cooling profiles, in agreement with previous results seen in PD96.

Accepted for publication in *Journal of the Atmospheric Sciences*. DOI10.1175/JAS-D-19-0347.1.

c. Environment modification

The environmental modifications ahead of each MCS early in each simulation are quite similar in gross characteristics across the hail and the graupel simulations. From Figs. 11 and 12 the stabilizing effects of the initial $n = 1$ waves produce approximately equivalent responses in the hail and graupel tests. As also seen in AS20, the initial $n = 1$ wave has a larger impact on the CAPE field as opposed to the LFC field: the peak velocity perturbations associated with $n = 1$ waves are in the mid-levels, which would more strongly impact CAPE. The initial latent heating perturbations are strongest in the stronger shear tests (Fig. 6), which explains why the associated vertical motions (Figs. 5e,f) and CAPE impacts (Figs. 11e,f) are also largest; a similar result is true for increasing instability. This early in the simulations, few differences between the hail and graupel simulations are seen among the latent heating or cooling profiles (Fig. 4), so the lack of differences in CAPE and LFC perturbations is unsurprising.

As the simulations progress past 60 min and all simulations have developed a stratiform region, subtle differences in the CAPE and LFC fields become more evident as multiple $n = 2$ and $n = 3$ waves are generated. The weak shear tests show few differences until the third $n = 2$ wave, which has a larger CAPE increase in 16.2G5 (Fig. 11b) than in 16.2H5 (Fig. 11a). 16.2G5 has larger latent cooling rates compared to 16.2H5 (c.f. Figs. 4a,b) as larger amounts of graupel descend below the melting level (Fig. 3). A stronger $n = 2$ wave response (c.f. Figs. 7c,f) and associated CAPE response is likely. In the middling and strong shear simulations, slightly stronger CAPE responses can be seen in 16.2G15 and 16.2G25, particularly when comparing the earlier generated $n = 2$ waves. Latent cooling at the generation time of these waves was more concentrated in in the mid-levels and near the melting level, unlike in the hail simulations (c.f. Figs. 4c, d and e, f). With cooling and hence wave-induced vertical motion perturbations more concentrated at that

Accepted for publication in *Journal of the Atmospheric Sciences*. DOI10.1175/JAS-D-19-0347.1.

level in the graupel simulations, stronger CAPE perturbations are consistent with these results. CAPE perturbations are also usually stronger in association with $n = 3$ wave modes than $n = 2$ wave modes due to associated vertical motions being farther aloft; these stronger perturbations can be seen in the two $n = 3$ wave modes generated in 16.2G15 (Fig. 11d).

Conversely, the perturbations in the LFC field associated with higher-order wave modes are slightly stronger in the hail simulations than the graupel simulations. Any differences in the weak shear tests are difficult to identify. However, in 16.2H15 and 16.2H25 (Figs. 12c,e) the LFC values immediately near the convective line during the 40-100 min period, the period during the generation of the majority of the $n = 2$ waves, are about 25-50 m lower than in the 16.2G15 and 16.2G25 tests (Figs. 12d,f). Again, latent cooling in the middling and strong shear hail simulations extended from the melting level to the surface (Figs. 4c,e); ing the graupel simulations cooling was more concentrated in the mid-levels. The generated waves and associated vertical motions thus were more concentrated in the lower levels in the hail simulations (c.f., Figs. 8i,l and o,r), so the hail simulations also had larger LFC perturbations.

d. MCS response

AS20 noted two separate regimes of MCS wave interaction and feedback in conjunction with updraft development and maintenance. During the developing stage of MCSs, AS20 found the low-frequency wave modifications to the CAPE and LFC fields in advance of the system to directly impact MCS updraft strength through destabilizing the inflow. After the development of the stratiform region and transition into the mature stage, MCS updraft maintenance appeared to be indirectly controlled by destabilizing low-frequency waves coupling with high-frequency waves to generate new convective cells in advance of the system. As those cells were advected into the

Accepted for publication in *Journal of the Atmospheric Sciences*. DOI10.1175/JAS-D-19-0347.1.

original convective line and absorbed, the extra moisture and latent heat reinvigorated the updraft, eventually generating new low-frequency waves and continuing the cycle.

During the MCS developing stage and prior to the development of the stratiform region, the vertical motion fields at both 2.5 and 6 km do not appear significantly different between the graupel and hail simulations (from initialization to about 40-70 minutes in Fig. 5). Nor do the CAPE and LFC fields appear significantly different before maturity and the generation of the second $n = 2$ wave (Figs. 11, 12). Thus, it would seem the first regime of low-frequency wave and MCS updraft intensity feedback are similar despite the microphysical parameterization differences. Figure 13 shows a modified version of Fig. 20 from AS20, now including the graupel tests via dashed lines. The notable features during the 0-70 min period prior to development of the stratiform region and during the MCS development stage (noted on Fig. 13 with arrows) are equally visible here: a significant lagged correlation between maximum updraft speed and CAPE at 4-10 min, and a leading correlation around 20 minutes. These features are indicative of the CAPE modifications in advance of the system feeding back and impacting the updraft intensity. After the MCSs reach maturity, the connection between maximum updraft speed and CAPE is no longer evident (Fig. 13b), again similar to AS20.

While the two low frequency wave - updraft interaction and feedback regimes appear generally unchanged despite the microphysical modifications, individual events of new cell development during the second feedback regime are affected. At first glance, the differences in responses in the LFC and CAPE fields between the hail and graupel simulations discussed in the previous section are subtle. However, as an MCS reaches maturity it reaches a stage of maintenance where its convective updraft is strengthened by development of discrete convective cells forming ahead of the convective line that are absorbed into the updraft, strengthening it (Fovell et al. 2006, AS20). The development of these discrete convective cells is tightly related to the LFC of the air immediately

Accepted for publication in *Journal of the Atmospheric Sciences*. DOI10.1175/JAS-D-19-0347.1.

ahead of the convective line as they are initialized by high-frequency gravity waves with small associated vertical velocity perturbations (Fovell et al. 2006, AS20). Thus, even small changes in the LFC can affect the initiation of these discrete convective cells, and hence mature MCS maintenance.

An example of the importance of these small differences in LFC between the hail and graupel simulations can be provided by the discrete propagation episode that occurs between 70 and 115 min in 16.2H15, but does not occur in 16.2G15. The evolution of the 1-km reflectivity and cloud water mixing ratio fields in both tests (Figs. 14a, b) reveals an extension of 1-km cloud water ahead of the convective line around 90 min in 16.2H15. Per Fig. 5i, it can be seen these clouds are originally generated by a passing $n = 2$ wave shortly after 70 min and advected toward the convective line by the low-level inflow. Additional clouds and finally reflectivity responses are evident shortly thereafter; as these features are absorbed into the convective line a peak in updraft speed as can be seen at 2.5 and 6 km (Figs. 5c, i). Conversely, test 16.2G15 shows no cloud or new cell development ahead of the convective line (Figs. 5j, 14b).

Around 70 min in the two simulations a higher order low-frequency wave was generated. In 16.2H15, an $n = 2$ and $n = 3$ wave were each generated. These waves are identified with arrows in Fig. 7i at X=95 km ($n = 3$) and X=107 km ($n = 2$). Note how the vertical motion response associated with the $n = 2$ wave extends from 6 km to below 1 km, while the response from the $n = 3$ wave is concentrated between 4 and 6 km. In 16.2G15, only an $n = 3$ wave is generated and can be seen in Fig. 7l at X=105 km. The vertical motion associated with that wave is concentrated between 4 and 6 km. The microphysical cooling tendencies within the stratiform region reveal the reason behind these differences: in 16.2H15 (Fig. 4c), the cooling extends from 6 km to the surface with the largest cooling rates peaking in the 1-4 km layer as the faster-falling hail falls a

Accepted for publication in *Journal of the Atmospheric Sciences*. DOI10.1175/JAS-D-19-0347.1.

longer distance while melting. In 16.2G15 (Fig. 4d), the cooling is concentrated in the 4-6 km layer with melting and sublimation the major contributing processes.

In this case, the deeper lifting associated with the $n = 2$ wave in 16.2H15, compared to the lifting more concentrated aloft associated with the $n = 3$ wave in 16.2G15, was able to lower the LFC up to 50 m more in 16.2H15 compared to 16.2G15 (Fig. 15). Small perturbations in the vertical wind field associated with high-frequency gravity waves were evident in the 2-4 km layer in both simulations (not shown). However, only in 16.2H15 with the more destabilized lower levels were these high-frequency perturbations able to grow upscale into new cell development. The vertical motion associated with each convective line after the absorption of the new cells (approximately 106 min simulation time) shows a stronger, wider updraft in 16.2H15 aided by the absorption of the new cells, some of which are still evident ahead of the line around X=100 km (c.f., Figs. 14c,d).

As was seen in AS20, development of new cells ahead of the convective line, advection of those cells toward the convective line, and finally absorption of those cells into the main convective updraft, led to a significant strengthening of that main updraft. Fig. 16 shows this relationship is evident across all the middling and high shear simulations in both hail and graupel tests. Development of new cloud or convective cells ahead of the convective line still appears tightly connected with generation of higher-order wave modes acting to destabilize the environment in advance of the system. (Note in Fig. 16 the lines denoting waves are copied from Fig. 5, from where they were originally identified.) From the previous example, it also appears the development of new convective cells is a delicate process that can be easily disrupted, depending on the structure and effectiveness of the destabilizing wave. The use of graupel instead of hail as a rimed ice class does not remove all episodes of new cell development, as it can still be seen in 16.2G25 (Fig. 16f). However, the sensitivity of multiple episodes of new cell development and subsequent convective restrengthening to the type of generated wave - and hence, the latent heating profile - suggests

Accepted for publication in *Journal of the Atmospheric Sciences*. DOI10.1175/JAS-D-19-0347.1.

careful examination of the microphysical parameterization is necessary to correctly simulate the appropriate low-frequency gravity waves and thereby fully understand the growth and maintenance mechanisms of an MCS.

5. Discussion and conclusions

In this study low-frequency gravity waves, generated within MCS simulations over a range of initial environmental instabilities and shear, were examined to determine the impact on these waves of changes in the parameterization of the dense rimed ice field from hail to graupel. The graupel simulations had wider, less intense convective lines with little distinction between the convective line and stratiform region. Hail simulations had more intense, narrower convective lines with less intense stratiform regions. The faster-falling hail resulted in lower magnitudes of mean and peak hail mixing ratios that were located over a deeper layer than in the graupel simulations. Additionally, the peak hail mixing ratios were more concentrated in the horizontal near the convective line, further resulting in lower overall mean hail mixing ratios. The largest differences were seen in the high shear simulations, as a result of the stronger storm-relative flow aloft advecting the hydrometeors over a longer distance.

Onset of cooling occurred slightly more quickly in hail simulations due to the faster fallspeeds of hail compared to graupel. Cooling rates, both in sum and by individual process, were larger in the graupel simulations than the hail simulations as they progressed, except in middling shear simulations where total cooling rates were larger in the hail simulations due to increased low-level evaporation. Cooling rates in the graupel simulations were generally concentrated in the 3-6 km layer, with a significant portion of the cooling coming from sublimation and melting. Cooling rates in the hail simulations were generally concentrated in the 2-4 km layer, with melting and evaporation being the largest contributing processes. However, while these general trends

Accepted for publication in *Journal of the Atmospheric Sciences*. DOI 10.1175/JAS-D-19-0347.1.

in the cooling profiles could be identified, the variability of each profile over the course of each simulation ensured there wasn't a specific "hail" or "graupel" cooling profile evident at all times.

Waves generated by an $n = 1$ vertical heating profile appeared during the developing portion of each simulation largely at the same time in both hail and graupel simulations. The first $n = 2$ waves, generated at the time precipitation first starts falling below the cloud base, were also largely similar in timing and strength in both hail and graupel simulations. As the simulations progressed the latent cooling profiles began to increasingly differ, and the strength, timing, and type of higher-order wave modes generated similarly diverged. However, specific wave modes were not limited to just hail or just graupel simulations. Instead, the type and strength of generated waves were tightly related to the cooling profile at that time in each simulation, which varied among the hail and graupel simulations depending on shear or instability.

The development of rear-to-front flow, its vertical distribution, and its descent to the surface appears tightly linked to the second and third $n = 2$ or $n = 3$ wave generated in each simulation by the changing latent cooling profiles at the time of and shortly after the development of the stratiform region. Depending on the distribution and tilt of the overall heating and cooling profile associated with the MCS, the resulting rear-to-front flow was either entirely elevated or descended to the surface farther behind the convective line, in a manner very similar to the results obtained by PD96. Entirely upright heating/cooling profiles resulted in elevated rear-to-front flow, seen early in all simulations by only in the strong shear simulations after maturity. The location of the vertical maximum of the rear-to-front flow appeared to depend on both the degree of tilt of the updraft and associated cooling, with stronger tilts having higher elevated vertical maximum again as in PD96. As the middling shear simulations progressed, the degree of tilt became more pronounced resulting in the rear-to-front flow descending to the surface farther behind the convective line. In 16.2G15 additional mid-level cooling generated an $n = 3$ wave mode that reduced the magnitude

Accepted for publication in *Journal of the Atmospheric Sciences*. DOI 10.1175/JAS-D-19-0347.1.

of the low- and mid-level flow, a potential extension of the work by PD96, but not evident in every graupel simulation. Again, as the cooling profiles did not have a uniform response across environments to the change from hail to graupel, the wave responses were similarly non-uniform but instead directly related to the variability seen among the cooling changes.

Initial perturbations in the CAPE and LFC fields show little difference among the hail and graupel simulations due to few difference. After the MCs reached maturity, however, the CAPE perturbations in the graupel simulations were generally larger than those of the hail simulations. Conversely, LFC perturbations in the hail simulations were generally larger than those of the graupel simulations. These differences can be attributed to the differences in the height of the peak cooling in hail versus graupel simulations; peak cooling located farther aloft closer to the melting level in the graupel simulations generally resulted in stronger vertical motion perturbations in the mid-levels as well. Such perturbations would have a stronger impact on the CAPE field than the LFC. These perturbations in the vertical distribution of cooling were apparently not of such large and uniform in magnitude to result in consistently different types of waves being generated in the hail and graupel simulations, but the differences did still cause consistently different impacts in the effects of the waves.

Examination of the MCS structure, updraft strength, and cloud water field over time in all simulations revealed that the two regimes of MCS wave interaction and feedback noted by AS20 were overall unchanged by the microphysical perturbations. Specifically, during the development stage and prior to the development of the stratiform region, updraft speed was directly modified by ingesting air modified by wave-generated CAPE perturbations. During maturity and after development of the stratiform region, updraft speed and intensity was indirectly modified by higher-order wave modes destabilizing the region in advance of the system, allowing high-frequency waves to generate new, discrete clouds or convective cells that had an intensifying effect upon the convec-

Accepted for publication in *Journal of the Atmospheric Sciences*. DOI10.1175/JAS-D-19-0347.1.

tive updraft once absorbed (similar to the discrete propagation mechanism of Fovell et al. (2006)). While the timing and major characteristics of the two regimes remained unchanged, specific discrete convection events were disrupted by differing low-frequency waves generated during the microphysical sensitivity tests. The small nature of the high frequency wave perturbations typically responsible for generating the new convective cell or cloud growth meant the process was highly sensitive to even subtle changes in the original destabilizing wave. Such a result indicates the importance of fully characterizing the microphysical cooling profile in order to be able to completely capture the MCS maintenance process.

Given the wide range of waves and subsequent responses seen in the idealized simulations both here and in AS20, it begs the question as to why these features have not been more regularly found in observational data. A few studies have found occasional instances of $n = 1$ and $n = 2$ waves (Adams-Selin and Johnson 2010; Bryan and Parker 2010; Trapp and Woznicki 2017), but it is likely the subtle nature of these waves, particularly at the surface where the densest network of observations is found, has precluded further study of these features. Future work on this project will seek to identify these waves using both surface and remote instrumentation aloft to connect these idealized studies with observational work.

Acknowledgments. This work was supported by National Science Foundation Grant AGS-1636667. High-performance computing support from Cheyenne (doi:10.5065/D6RX99HX) was provided by NCAR's Computational and Information Systems Laboratory, sponsored by the National Science Foundation. All simulation data is archived and available via request. The helpful comments of three anonymous reviewers were greatly appreciated.

Accepted for publication in *Journal of the Atmospheric Sciences*. DOI10.1175/JAS-D-19-0347.1.

References

Adams-Selin, R., S. C. van den Heever, and R. H. Johnson, 2013a: Sensitivity of bow-echo simulation to microphysical parameterizations. *Wea. Forecasting*, **28**, 1188–1209.

Adams-Selin, R. D., 2020: Impact of convectively generated low-frequency gravity waves on Evolution of a Mesoscale Convective System. *J. Atmos. Sci.*, *accepted pending revisions*.

Adams-Selin, R. D., and R. H. Johnson, 2010: Mesoscale surface pressure and temperature features associated with bow echoes. *Mon. Wea. Rev.*, **138**, 212–227.

Adams-Selin, R. D., S. C. van den Heever, and R. H. Johnson, 2013b: Impact of graupel parameterization schemes on idealized bow echo simulations. *Mon. Wea. Rev.*, **141 (4)**, 1241–1262.

Bretherton, C. S., and P. K. Smolarkiewicz, 1989: Gravity waves, compensating subsidence and detrainment around cumulus clouds. *J. Atmos. Sci.*, **46 (6)**, 740–759, doi:10.1175/1520-0469(1989)046⟨0740:GWCSAD⟩2.0.CO;2.

Bryan, G., and J. Fritsch, 2002: A benchmark simulation for moist nonhydrostatic numerical models. *Mon. Wea. Rev.*, **130**, 2917–2928.

Bryan, G., and H. Morrison, 2012: Sensitivity of a simulated squall line to horizontal resolution and parameterization of micophysics. *Mon. Wea. Rev.*, **140**, 202–225.

Bryan, G. H., and M. D. Parker, 2010: Observations of a squall line and its near environment using high-frequency rawinsonde launches during vortex2. *Monthly Weather Review*, **138 (11)**, 4076–4097.

Cohen, C., and E. W. McCaul, 2006: The sensitivity of simulated convective storms to variations in prescribed single-moment microphysics parameters that describe particle distributions, sizes, and numbers. *Monthly Weather Review*, **134 (9)**, 2547–2565.

Accepted for publication in *Journal of the Atmospheric Sciences*. DOI10.1175/JAS-D-19-0347.1.

Fovell, R., 2002: Upstream influence of numerically simulated squall-line storms. *Quart. J. Roy. Meteor. Soc.*, **128**, 893–912.

Fovell, R., G. L. Mullendore, and S. Kim, 2006: Discrete propagation in numerically simulated nocturnal squall lines. *Mon. Wea. Rev.*, **134**, 3735–3752.

Fovell, R., and Y. Ogura, 1988: Numerical simulation of a mid-latitude squall line in two dimensions. *J. Atmos. Sci.*, **45**, 3846–3879.

Gallus, W. A., and R. H. Johnson, 1991: Heat and moisture budgets of an intense midlatitude squall line. *J. Atmos. Sci.*, **48**, 122–146.

Jensen, A. A., J. Y. Harrington, and H. Morrison, 2018: Microphysical characteristics of squall-line stratiform precipitation and transition zones simulated using an ice particle property-evolving model. *Monthly Weather Review*, **146 (3)**, 723–743, doi:10.1175/MWR-D-17-0215.1.

Lane, T., and M. J. Reeder, 2001: Convectively generated gravity waves and their effect on the cloud environment. *J. Atmos. Sci.*, **58**, 2427–2440.

Mapes, G., 1993: Gregarious tropical convection. *J. Atmos. Sci.*, **50**, 2026–2037.

Marinescu, P., S. van den Heever, S. M. Saleeby, and S. M. Kreidenweis, 2016: The microphysical contributions to and evolution of latent heating profiles in two MC3E MCSs. *J. Geophys. Res.*, **121**, 7913–7935.

Morrison, H., and J. Milbrandt, 2011: Comparison of two-moment bulk microphysics schemes in idealized supercell thunderstorm simulations. *Mon. Wea. Rev.*, **139**, 1103–1130.

Morrison, H., J. A. Milbrandt, G. H. Bryan, K. Ikeda, S. A. Tessendorf, and G. Thompson, 2015a: Parameterization of cloud microphysics based on the prediction of bulk ice particle properties.

Accepted for publication in *Journal of the Atmospheric Sciences*. DOI10.1175/JAS-D-19-0347.1.

Part II: Case study comparisons with observations and other schemes. *Journal of the Atmospheric Sciences*, **72**, 312–339.

Morrison, H., A. Morales, and C. Villanueva-Birriel, 2015b: Concurrent sensitivities of an idealized deep convective storm to parameterization of microphysics, horizontal grid resolution, and environmental static stability. *Monthly Weather Review*, **143**, 2082–2104.

Morrison, H., G. Thompson, and V. Tatarskii, 2009: Impact of cloud microphysics on the development of trailing stratiform precipitation in a simulated squall line: Comparison of one- and two-moment schemes. *Mon. Wea. Rev.*, **137**, 991–1007.

Nicholls, M., 1987: A comparison of the results of a two-dimensional numerical simulation of a tropical squall line with observations. *Mon. Wea. Rev.*, **115**, 3055–3077.

Nicholls, M., R. A. Pielke, and W. R. Cotton, 1991: Thermally forced gravity waves in an atmosphere at rest. *J. Atmos. Sci.*, **48**, 1869–1884.

Pandya, R., D. Durran, and C. Bretherton, 1993: Comments on "Thermally forced gravity waves in an atmosphere at rest". *J. Atmos. Sci.*, **50**, 4097–4101.

Pandya, R., D. Durran, and M. Weisman, 2000: The influence of convective thermal forcing on the three-dimensional circulation around squall lines. *J. Atmos. Sci.*, **57**, 29–45.

Pandya, R. E., and D. R. Durran, 1996: The influence of convectively generated thermal forcing on the mesoscale circulation around squall lines. *J. Atmos. Sci.*, **53 (20)**, 2924–2951.

Pettet, C. R., and R. H. Johnson, 2003: Airflow and precipitation structure of two leading stratiform mesoscale convective systems determined from operational datasets. *Weather and Forecasting*, **18 (5)**, 685–699.

Accepted for publication in *Journal of the Atmospheric Sciences*. DOI10.1175/JAS-D-19-0347.1.

Pu, Z., C. Lin, X. Dong, and S. Krueger, 2018: Sensitivity of numerical simulations of a mesoscale convective system to ice hydrometeors in bulk microphysical parameterization. *Pure and Applied Geophysics*, **176**.

Shige, S., and T. Satomura, 2001: Westward generation of eastward-moving tropical convective bands in TOGA COARE. *J. Atmos. Sci.*, **58**, 3724–3740.

Stephan, C., M. J. Alexander, and J. H. Richter, 2016: Characteristics of gravity waves from convection and implications for their parameterization in global circulation models. *Journal of the Atmospheric Sciences*, **73 (7)**, 2729–2742.

Szeto, K., and H. Cho, 1994: A numerical investigation of squall lines. Part III: Sensitivity to precipitation processes and the Coriolis force. *J. Atmos. Sci.*, **51**, 1341–1351.

Trapp, R., and J. Woznicki, 2017: Convectively induced stabilizations and subsequent recovery with supercell thunderstorms during the Mesoscale Predictability Experiment (MPEX). *Mon. Wea. Rev.*, **145**, 1739–1754.

van den Heever, S. C., and W. R. Cotton, 2004: The impact of hail size on simulated supercell storms. *J. Atmos. Sci.*, **61**, 1596–1609.

Van Weverberg, K., 2013: Impact of environmental instability on convective precipitation uncertainty associated with the nature of the rimed ice species in a bulk microphysics scheme. *Monthly Weather Review*, **141 (8)**, 2841–2849.

Van Weverberg, K., N. van Lipzig, and L. Delobbe, 2011: The impact of size distribution assumptions in a bulk one-moment microphysics scheme on simulated surface precipitation and storm dynamics during a low-topped supercell case in Belgium. *Monthly Weather Review*, **139**, 1131–1147.

Accepted for publication in *Journal of the Atmospheric Sciences*. DOI10.1175/JAS-D-19-0347.1.

Van Weverberg, K., A. Voglemann, H. Morrison, and J. Milbrandt, 2012: Sensitivity of idealized squall-line simulations to the level of complexity used in two-moment bulk microphysics schemes. *Monthly Weather Review*, **140**, 1883–1907.

Weisman, M., and J. Klemp, 1982: The dependence of numerically simulated convective storms on vertical wind shear and buoyancy. *Mon. Wea. Rev.*, **110**, 504–520.

Weisman, M., W. Skamarock, and J. Klemp, 1997: The resolution dependence of explicitly modeled convective systems. *Mon. Wea. Rev.*, **125**, 527–548.

Yang, M., and R. H. Jr., 1995: Sensitivity of squall-line rear inflow to ice microphysics and environmental humidity. *Mon. Wea. Rev.*, **123**, 3175–3193.

Yuter, S. E., and R. A. Houze, 1995: Three-dimensional kinematic and microphysical evolution of Florida cumulonimbus. Part I: Spatial distribution of updrafts, downdrafts, and precipitation. *Monthly Weather Review*, **123 (7)**, 1921–1940.

Accepted for publication in *Journal of the Atmospheric Sciences*. DOI10.1175/JAS-D-19-0347.1.

LIST OF TABLES

Accepted for publication in *Journal of the Atmospheric Sciences*. DOI 10.1175/JAS-D-19-0347.1.

TABLE 1. Sensitivity test simulation names.

Simulation name name	Surface q_v (g kg^{-1})	MUCAPE (J kg^{-1})	0-5 km shear (m s^{-1})	rimed ice class
14.3H5	14.3	2497	5	hail
16.2H5	16.2	3538	5	hail
14.3H15	14.3	2497	15	hail
16.2H15	16.2	3538	15	hail
14.3H25	14.3	2497	25	hail
16.2H25	16.2	3538	25	hail
14.3G5	14.3	2497	5	graupel
16.2G5	16.2	3538	5	graupel
14.3G15	14.3	2497	15	graupel
16.2G15	16.2	3538	15	graupel
14.3G25	14.3	2497	25	graupel
16.2G25	16.2	3538	25	graupel

Accepted for publication in *Journal of the Atmospheric Sciences*. DOI10.1175/JAS-D-19-0347.1.

LIST OF FIGURES

Accepted for publication in *Journal of the Atmospheric Sciences*. DOI10.1175/JAS-D-19-0347.1.

Accepted for publication in *Journal of the Atmospheric Sciences*. DOI10.1175/JAS-D-19-0347.1.

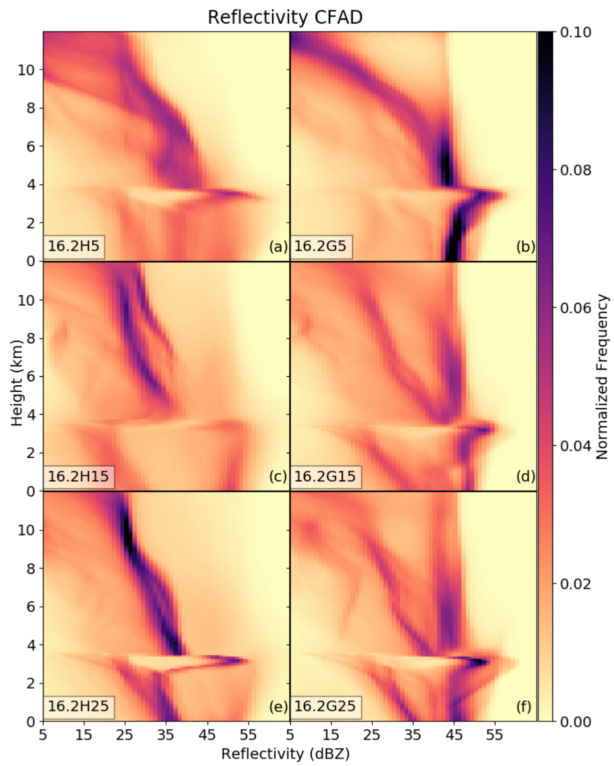

806 FIG. 1. Contoured Frequency by Altitude Diagram (CFAD; Yuter and Houze (1995)) for the shear simulations as labelled. Hail (graupel) simulations are in the left (right) column; rows show simulations with increasing amounts of shear. Frequency shown is the frequency of occurrence of various reflectivities at that height over the course of the 2.5-h simulation for the X cross section from Y=120 to 130 km, normalized by the total occurrence of all reflectivities at that height.

Accepted for publication in *Journal of the Atmospheric Sciences*. DOI10.1175/JAS-D-19-0347.1.

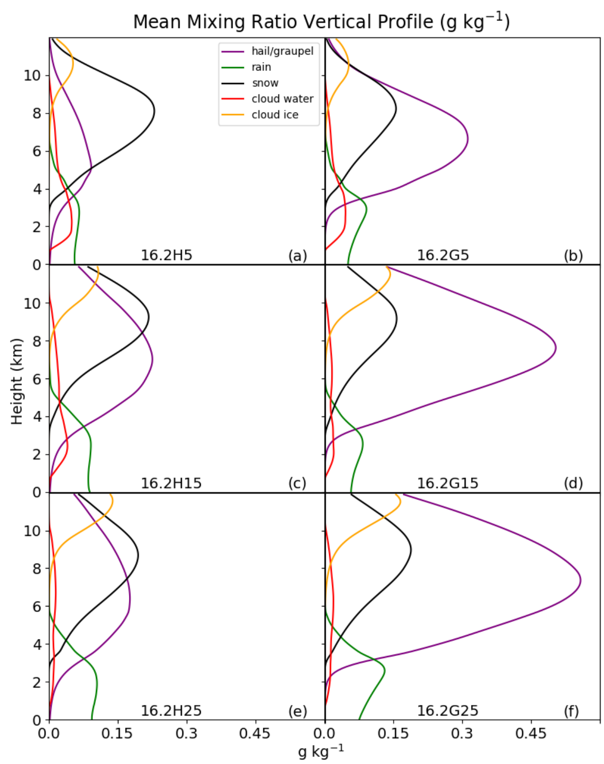

811 FIG. 2. Vertical profiles of mean hydrometeor mixing ratios (g kg^{-1}) over the horizontal domain and time
812 duration of each shear simulation, as labelled, for the same cross section as in Fig. 1.

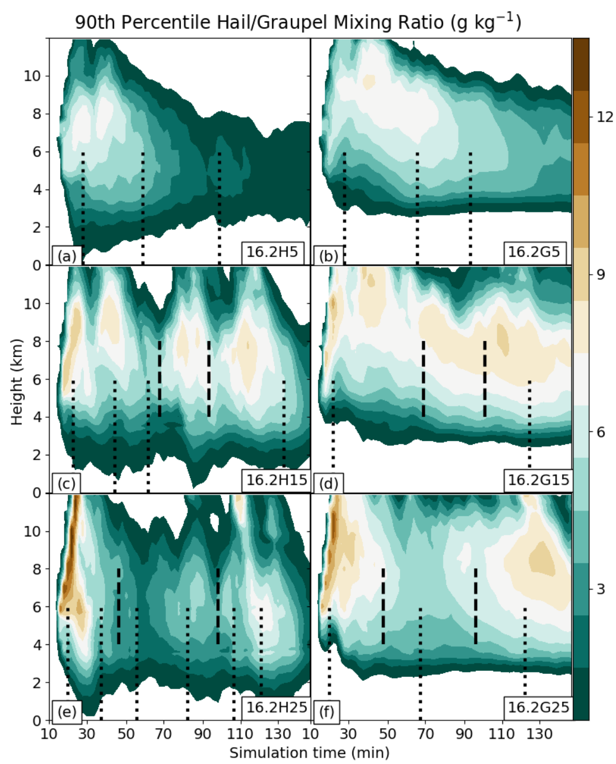

FIG. 3. Time-height evolution of the 90th percentile of the hail or graupel hydrometeor mixing ratio (g kg^{-1}) for the shear simulations as labelled. Dashed and dotted vertical lines represent generation times of $n = 2$ and $n = 3$ waves, respectively.

Accepted for publication in *Journal of the Atmospheric Sciences*. DOI10.1175/JAS-D-19-0347.1.

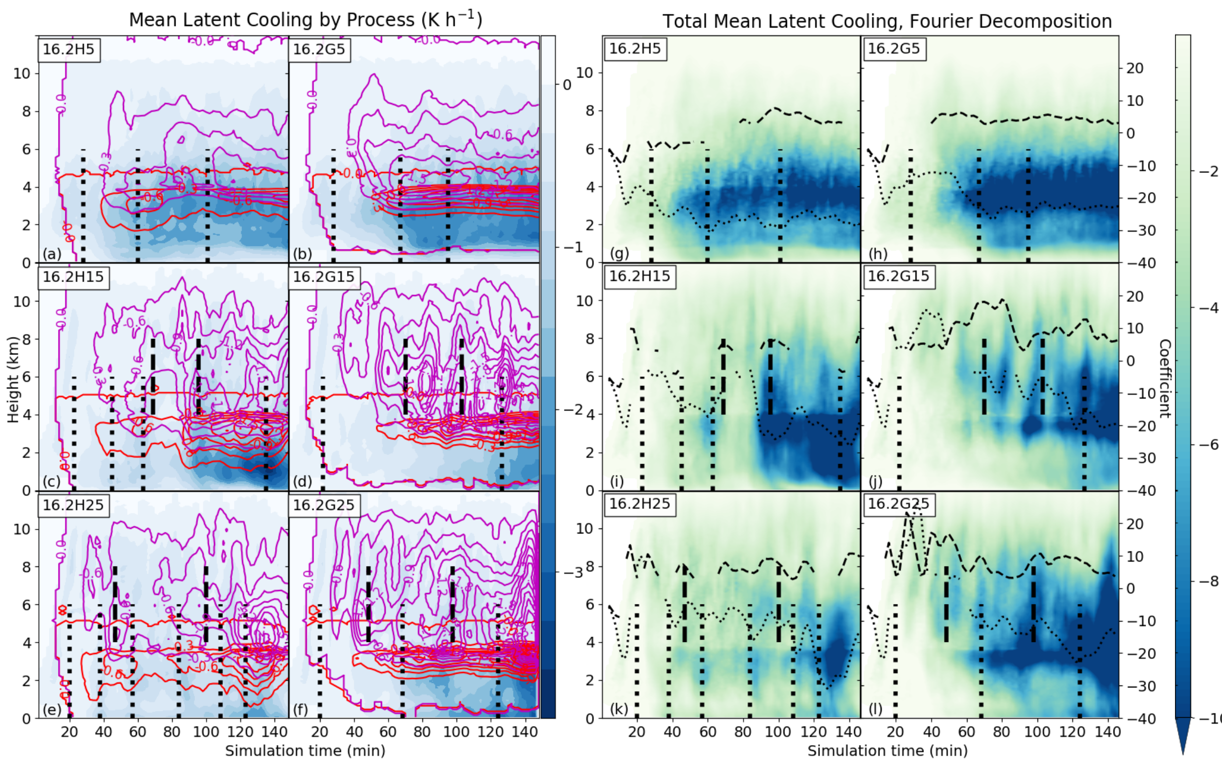

FIG. 4. (a-f) Time-height evolution of mean latent cooling (K h^{-1}) by process for the same cross-section as in Fig. 1 for the shear simulations as labelled. Evaporation (blue color fill), melting (red contour; -0.3 K h^{-1}), and sublimation (purple contour; -0.3 K h^{-1}). (g-l) Time-height evolution of mean latent cooling of all processes in sum. The line plots are the coefficients from a Fourier decomposition of the mean cooling profile for $n = 2$ (dotted) and $n = 3$ (dashed) profiles. Line only shown if the coefficient is determined to be significant per a two-tailed t-test and the entire decomposition is significant per the F-statistic. In all subfigures vertical dotted and dashed lines are generation times of $n = 2$ and $n = 3$ waves, as in Fig. 3.

Accepted for publication in *Journal of the Atmospheric Sciences*. DOI10.1175/JAS-D-19-0347.1.

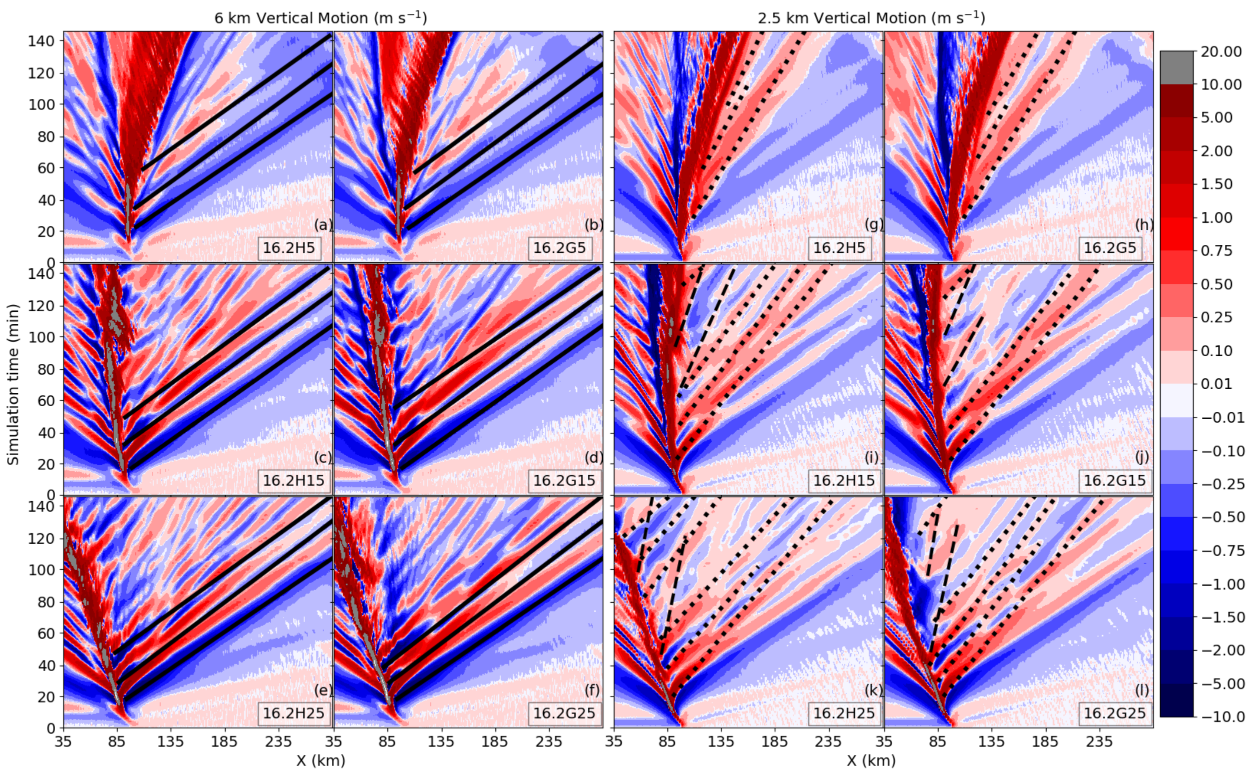

823 FIG. 5. Hovmöller diagrams of vertical motion (m s^{-1}) at (a-f) 6 km and (g-l) 2.5 km for the shear simulations
824 as labelled. Identified $n = 1$, $n = 2$, and $n = 3$ gravity waves denoted by solid black lines, dotted lines, and dashed
825 lines, respectively.

Accepted for publication in *Journal of the Atmospheric Sciences*. DOI10.1175/JAS-D-19-0347.1.

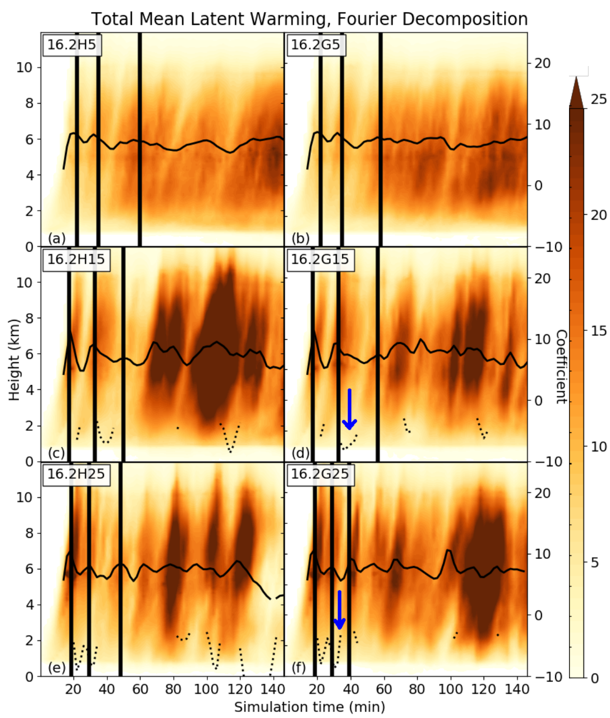

FIG. 6. (a-f) Time-height evolution of total mean latent warming (K h^{-1}) for the same cross-sections and simulations as in Fig. 4, as labeled. The solid and dotted line plots are coefficients from a Fourier decomposition of the mean heating profile for $n = 1$ and $n = 2$ profiles; line only shown if the coefficient is determined to be significant per a two-tailed t-test, and the entire decomposition is significant per the F-statistic. In all subfigures solid vertical lines are generation times of $n = 1$ waves. Blue arrows point to generation time of $n = 2$ waves discussed in the text.

.

Accepted for publication in *Journal of the Atmospheric Sciences*. DOI10.1175/JAS-D-19-0347.1.

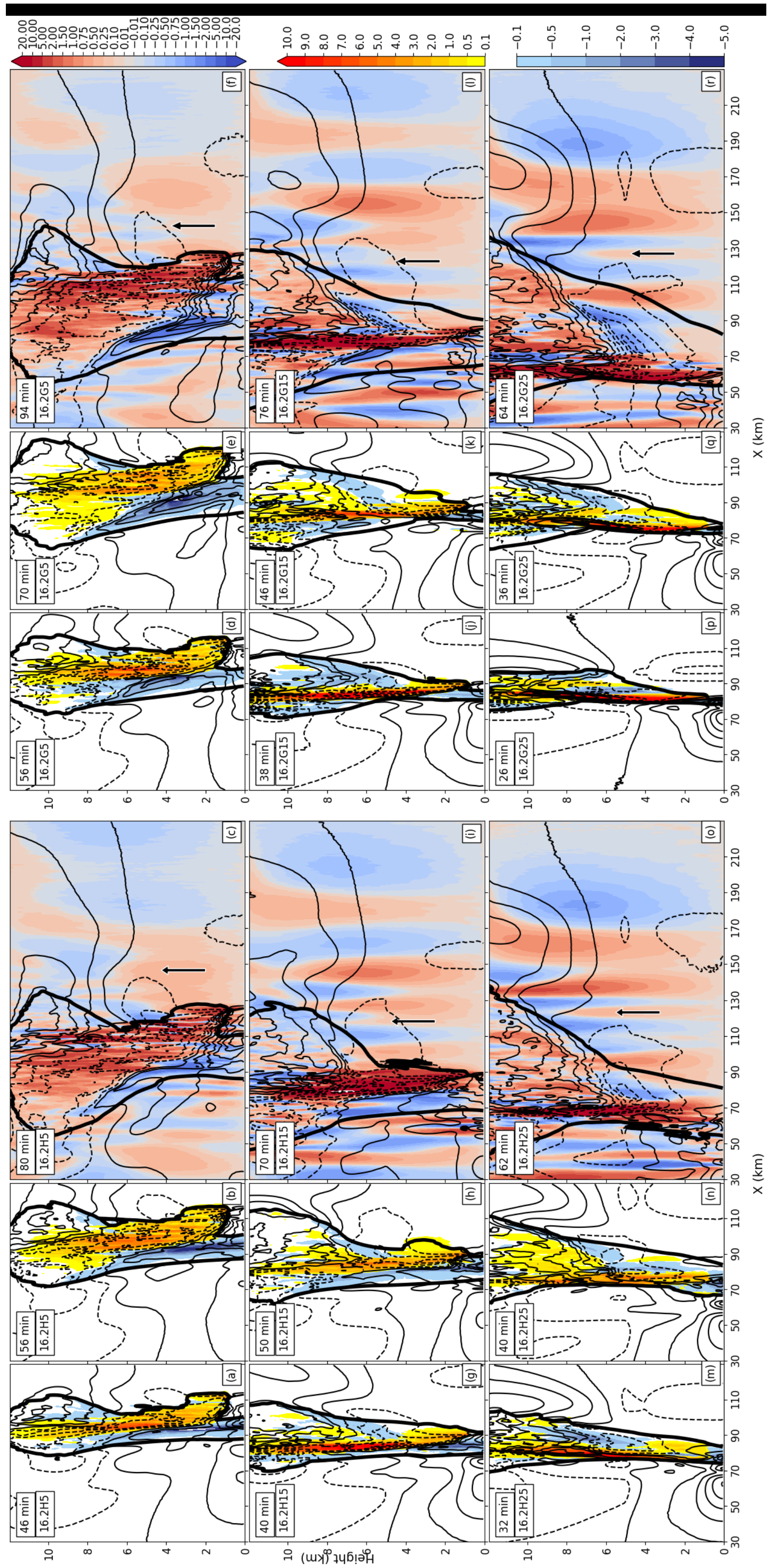

Accepted for publication in *Journal of the Atmospheric Sciences*. DOI10.1175/JAS-D-19-0347.1.

FIG. 7. (1st, 2nd, 4th, and 5th columns) Vertical cross-sections of latent heating (K h^{-1}; yellow-red color fill), latent cooling (K h^{-1}; blue color fill), u wind perturbation (black line every 4 m s^{-1}, negative dashed), and total condensate (0.1 g kg^{-1}; thick black line). (3rd, 6th column) Vertical cross-sections of vertical motion (m s^{-1}; blue-red color fill), u wind perturbation (black line every 4 m s^{-1}, negative dashed), and total condensate (0.1 g kg^{-1}; thick black line). Left three columns are hail simulations, right three columns are graupel simulations, as labelled. Rows correspond to simulations with increasing shear. The three subfigures from each simulation show the times before (e.g., (a)) and after (e.g., (b)) generation of the 2nd $n = 2$ wave and initial development of stratiform precipitation. Third figure (e.g., (c)) shows the resulting wave or waves in the vertical motion field highlighted with a black arrow.

Accepted for publication in *Journal of the Atmospheric Sciences*. DOI10.1175/JAS-D-19-0347.1.

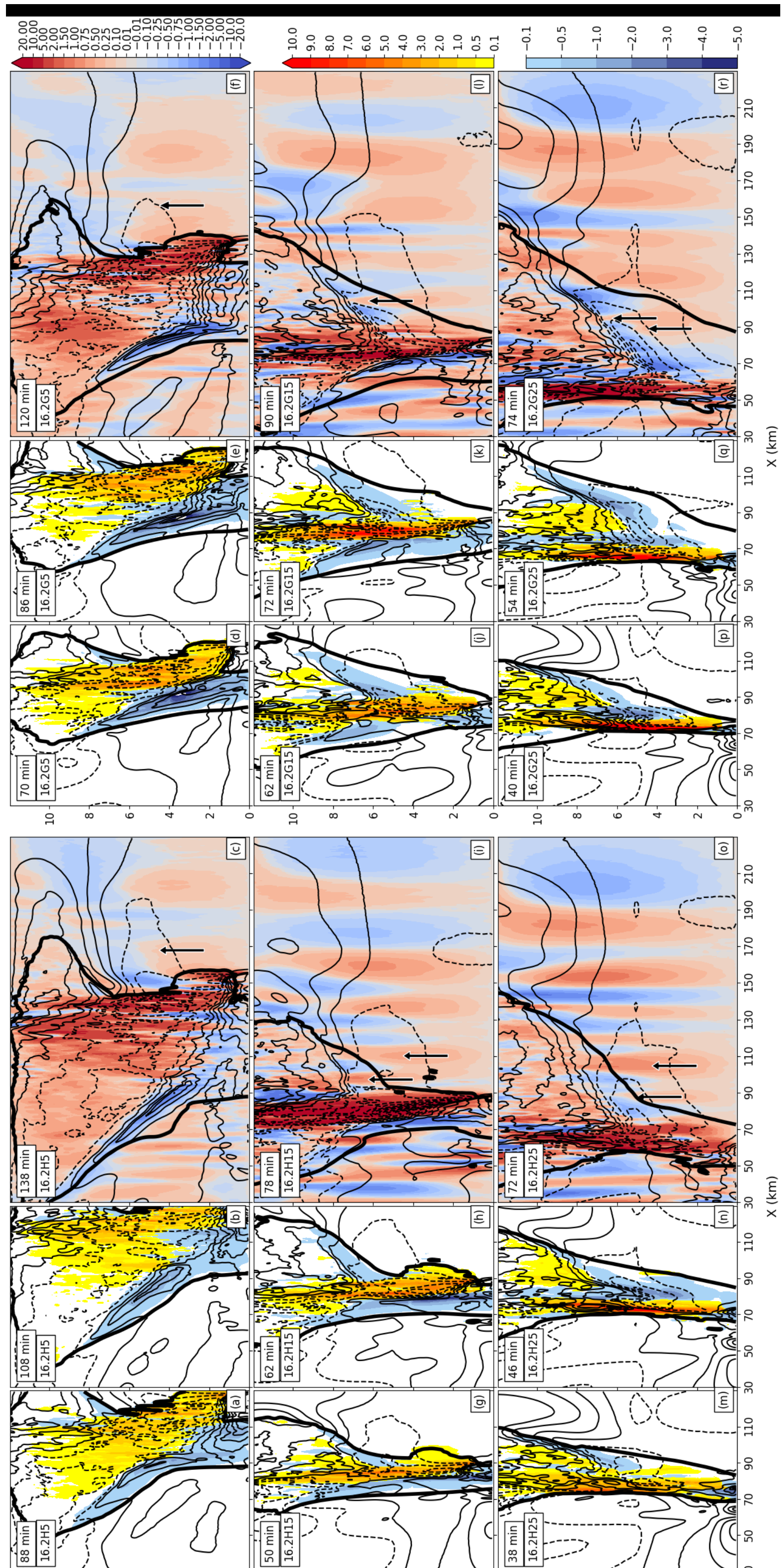

Accepted for publication in *Journal of the Atmospheric Sciences*. DOI10.1175/JAS-D-19-0347.1.

FIG. 8. As in Fig. 7, but the three subfigures from each simulation show the times before (e.g., (a)) and after (e.g., (b)) generation of the 3rd higher-order wave and intensification of rear inflow, and (e.g., (c)) the resulting wave in the vertical motion field highlighted with an arrow.

Accepted for publication in *Journal of the Atmospheric Sciences*. DOI10.1175/JAS-D-19-0347.1.

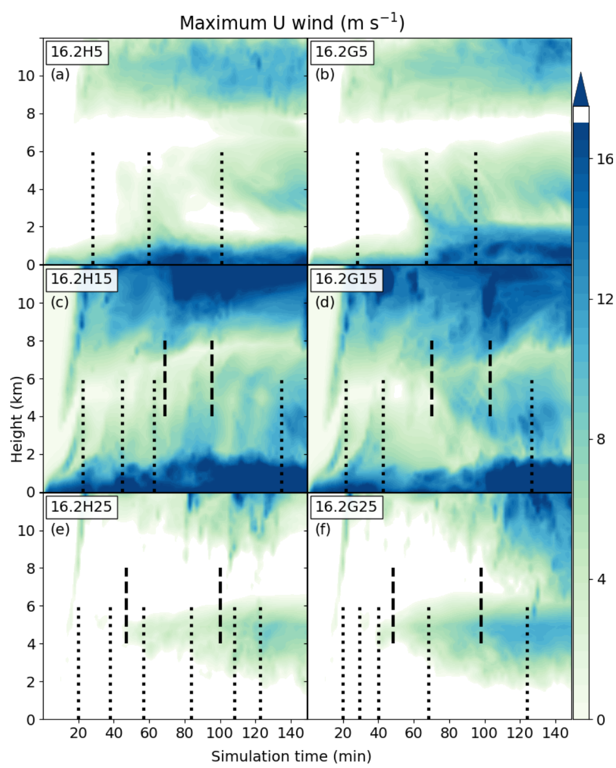

FIG. 9. Time-height evolution of vertical profiles of maximum rear-to-front storm-relative u wind speed (m s^{-1}). Rear-to-front flow in (e,f) travels from the east (larger x values). Dotted lines are generation times of $n = 2$ waves; dashed lines generation times of $n = 3$ waves as in Fig. 4.

Accepted for publication in *Journal of the Atmospheric Sciences*. DOI10.1175/JAS-D-19-0347.1.

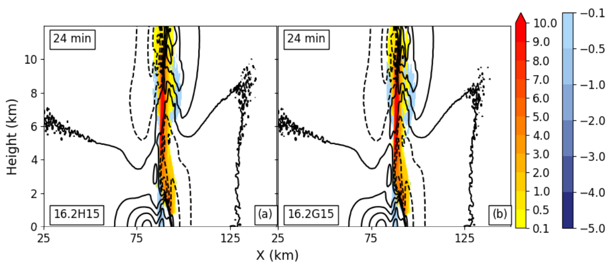

FIG. 10. Vertical cross-section of changes in temperature due to latent heating (warm color fill, K (h^{-1}) or cooling (blue color fill, K (h^{-1}) and u wind (black, 4 m s^{-1}, negative dashed) at the time (upper left) of the generation of the 1st $n = 2$ wave in 16.2H15 and 16.2G15.

Accepted for publication in *Journal of the Atmospheric Sciences*. DOI10.1175/JAS-D-19-0347.1.

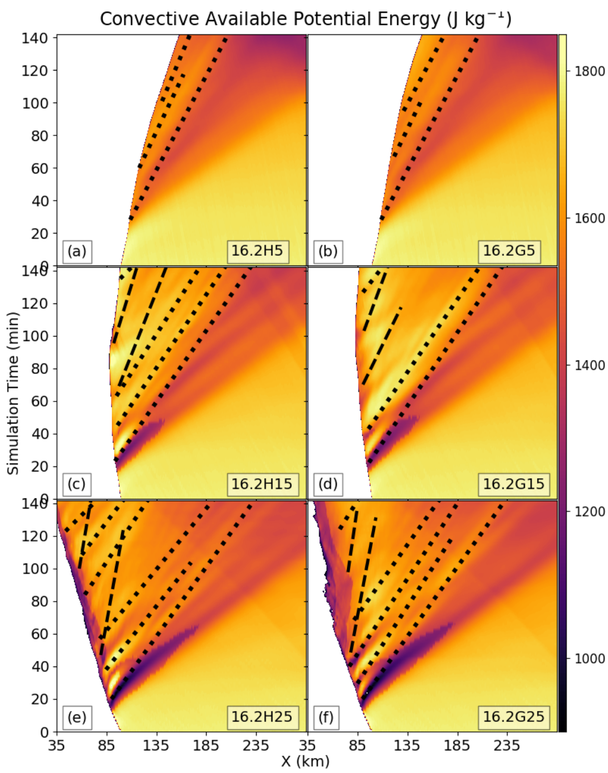

850 FIG. 11. Hovmöller diagrams of CAPE (J kg^{-1}) for the shear simulations as labelled. Identified $n = 2$ and
851 $n = 3$ gravity waves are as in Fig. 5.

Accepted for publication in *Journal of the Atmospheric Sciences*. DOI10.1175/JAS-D-19-0347.1.

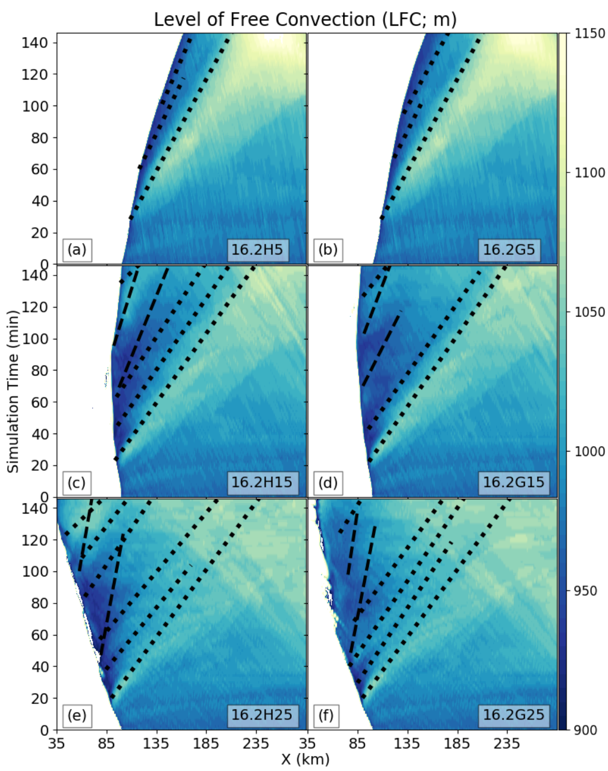

FIG. 12. As in Fig. 11, but for LFC (m).

Accepted for publication in *Journal of the Atmospheric Sciences*. DOI10.1175/JAS-D-19-0347.1.

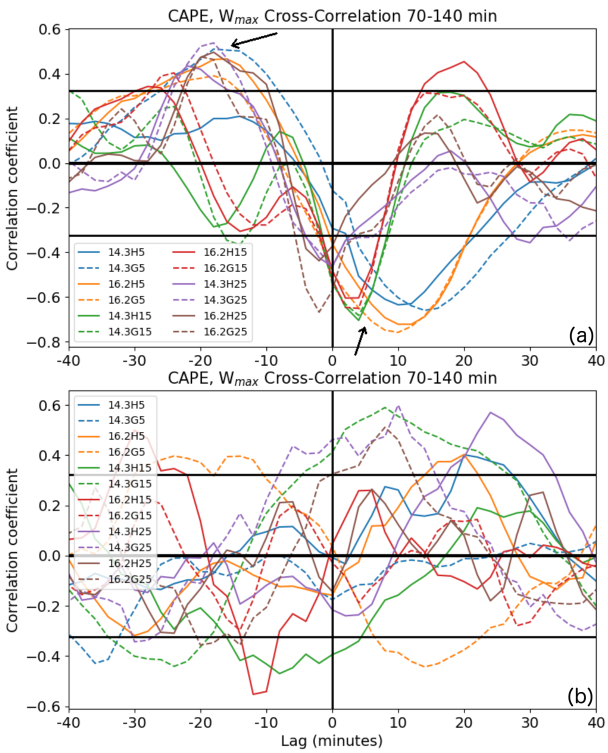

852 FIG. 13. Cross-correlation coefficients for all between surface-based CAPE (J kg^{-1}) 2.5 km ahead of the cold pool and maximum updraft speed for a range of positive and negative time lags. In a negative time lag an increase in CAPE precedes an increase in maximum updraft speed; in a positive time lag an increase in maximum updraft speed precedes an increase in CAPE. The thick solid horizontal lines delineate coefficients of at least 95% significance, as determined by a two-tailed t-test with over 30 degrees of freedom. (a) Coefficients between 0-70 minutes of the simulation, (b) between 70 and 140 min of the simulation.

Accepted for publication in *Journal of the Atmospheric Sciences*. DOI10.1175/JAS-D-19-0347.1.

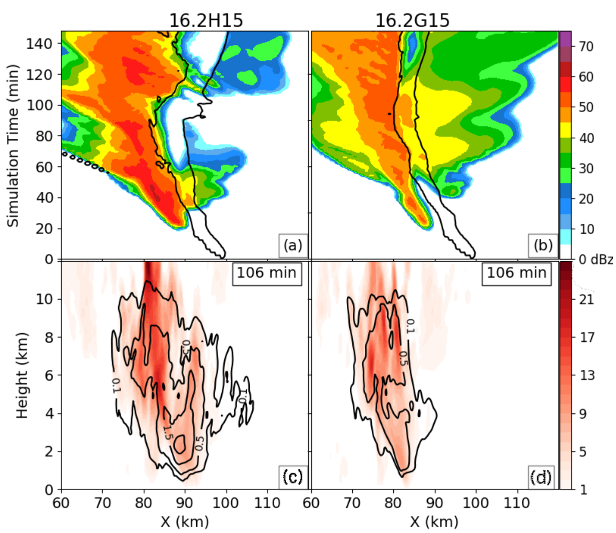

FIG. 14. Comparison of 16.2H15 (left column) and 16.2G15 (right column) immediately prior to and after an instance of discrete propagation. (a,b) Hovmöller diagrams of 1-km radar reflectivity (colors, dBZ) and cloud water mixing ratio (black, 0.1 g kg^{-1}). The discrete propagation event in question occurred shortly before 110 min in 16.2H15, and did not occur in 16.2G15. (c,d) Vertical cross-section of vertical motion (color, m s^{-1}) and cloud water mixing ratio (black, 0.5 g kg^{-1}) after absorption of the newly developed discrete cells at 106 min.

Accepted for publication in *Journal of the Atmospheric Sciences*. DOI10.1175/JAS-D-19-0347.1.

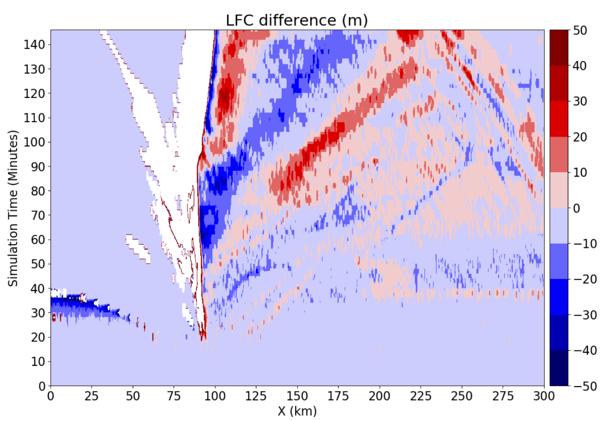

FIG. 15. Hovmöller diagram showing the difference in LFC values (m) between 16.2H15 and 16.2G15.

Accepted for publication in *Journal of the Atmospheric Sciences*. DOI10.1175/JAS-D-19-0347.1.

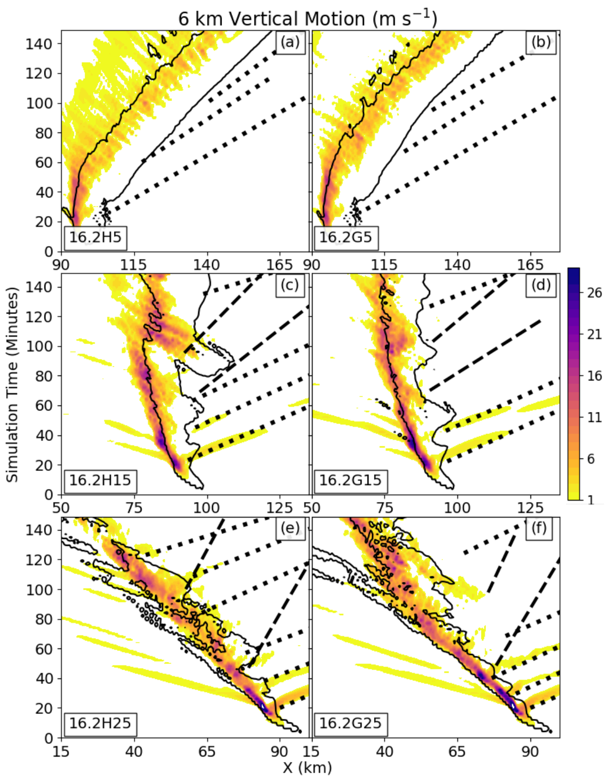

FIG. 16. Hovmöller diagrams of vertical motion at 6 km (color) and cloud water mixing ratio (black; 0.1 g kg^{-1}) for the shear simulations as labelled. X axes vary from (a-b) 65-175 km, (c-d) 50-135 km, and (e-f) 15-100 km. Identified $n = 1$, $n = 2$, and $n = 3$ gravity waves denoted by solid black lines, dotted lines, and dashed lines, respectively, and copied from Fig. 5, where they were originally identified.

Accepted for publication in *Journal of the Atmospheric Sciences*. DOI10.1175/JAS-D-19-0347.1.